

# Qubit Noise Sensing via Induced Photon Loss in a High-Quality Superconducting Cavity

Nitzan Kahn,\* Dror Garti,\* Uri Goldblatt, Lalit M. Joshi, Fabien Lafont, and Serge Rosenblum  
*Department of Condensed Matter Physics, Weizmann Institute of Science, Rehovot, Israel*

Characterizing the noise affecting superconducting qubits is essential for improving their performance. Existing noise-sensing techniques use the qubit itself as a detector, but its short coherence time limits both sensitivity and accessible frequency range. Here, we demonstrate a method for measuring qubit frequency noise by converting it into photon loss in a coupled high-quality superconducting cavity. We prepare a single photon in the cavity and perform repeated mid-circuit qubit measurements with post-selection to isolate noise-induced loss from intrinsic cavity decay, placing an upper bound on the intrinsic dressed-dephasing rate of  $(0.29\text{s})^{-1}$  at 508 MHz, corresponding to a qubit frequency-noise power spectral density below  $5.4 \times 10^3 \text{ Hz}^2/\text{Hz}$ . By exploiting the cavity's millisecond-scale lifetime, this technique provides access to high-frequency noise processes that are beyond the reach of conventional qubit-based spectroscopy and that may impose previously unexplored limits on qubit coherence.

Superconducting qubits couple strongly to their electromagnetic environment, making them susceptible to noise sources that induce energy relaxation and dephasing. These sources include voltage and current fluctuations in control circuitry, quasiparticle tunneling [1], and electric and magnetic field fluctuations associated with microscopic two-level system (TLS) defects [2]. Identifying and characterizing such noise processes is central to advancing qubit performance.

Standard noise detection methods, such as Ramsey interferometry [3], dynamical decoupling [4–6], and spin locking [7, 8], use the qubit itself as a probe [9–11]. However, these techniques are intrinsically limited by the qubit's coherence time, which restricts both their sensitivity and their accessible frequency range.

Superconducting high-quality-factor (high- $Q$ ) cavities offer a complementary platform [12–14]. Such cavities have proven highly effective for precision sensing [15, 16], notably in axion and dark photon dark matter searches, where they serve as resonant detectors for weak microwave signals [17–22]. Recent advances [23–25] have enabled these cavities to achieve millisecond-scale photon lifetimes when integrated with chip-based superconducting qubits [26, 27], making them natural candidates for sensitive characterization of qubit noise.

In this work, we use a high- $Q$  cavity to probe frequency noise in a chip-based superconducting qubit (see Fig. 1a). Our approach uses dressed dephasing, in which qubit frequency noise drives energy exchange between the cavity and the qubit, opening an additional photon loss channel whose rate is proportional to the frequency-noise spectral density at the cavity-qubit detuning [28, 29]. Previous work characterized this effect by driving a low- $Q$  resonator and observing qubit heating [30]. Here, we instead prepare a single photon in a millisecond-lifetime cavity and directly monitor its loss — inverting the roles of source and probe so that sensitivity is set by the cavity lifetime rather than the qubit coherence time. We perform repeated mid-circuit qubit measurements and post-select on the outcomes. This procedure isolates photon loss events associated with qubit noise from intrinsic cavity decay, enabling a quantitative measurement of

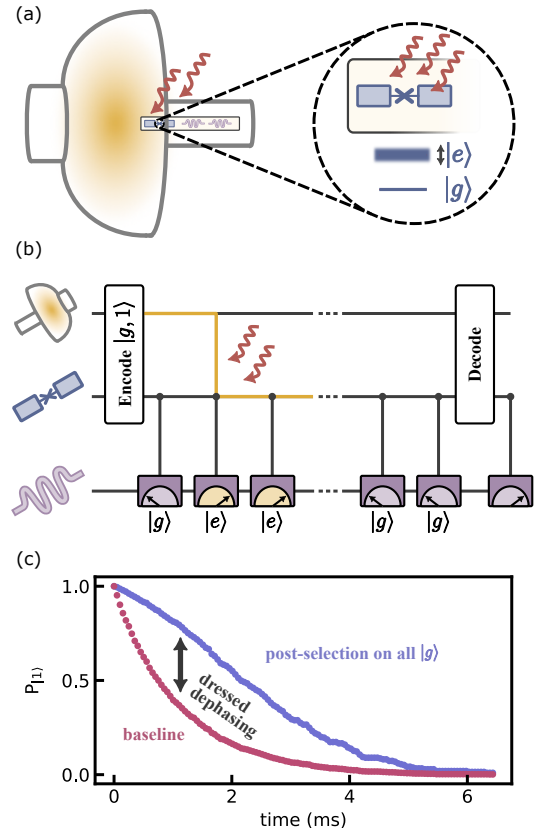


FIG. 1. Detecting transmon frequency noise with a high- $Q$  cavity. (a) Experimental setup. A half-elliptical cavity is coupled to a transmon chip subject to frequency noise (red arrows), corresponding to fluctuations in the transmon's resonance frequency. (b) The sensing protocol. A single photon is initialized in the cavity and the transmon is repeatedly measured during the cavity evolution. In a dressed dephasing event (red arrows), the cavity excitation is transferred to the transmon and detected by a subsequent measurement. Finally, the cavity population is mapped back onto the transmon and read out. (c) Simulated protocol output. The baseline cavity decay curve (pink) includes all measurement outcomes and decays at the total loss rate  $\kappa$ . The post-selected curve (purple), conditioned on all  $|g\rangle$  outcomes, decays more slowly because detected photon loss events have been discarded. The dressed dephasing rate  $\kappa_{\text{dd}}$  is extracted by comparing both curves.

\* These authors contributed equally to this work.

the noise. We validate the method by injecting controlled frequency noise and measuring the cavity lifetime response as a function of noise amplitude. Applying the protocol without added noise yields no resolvable dressed-dephasing signal, constraining the intrinsic rate to  $\kappa_{\text{dd}} < (0.29 \text{ s})^{-1}$  and the corresponding frequency-noise power spectral density (PSD) to  $S_{\delta\omega}(\Delta) < 5.4 \cdot 10^3 \text{ Hz}^2/\text{Hz}$ , at  $\Delta = 508 \text{ MHz}$ . This approach extends noise spectroscopy beyond the bandwidth of standard qubit-based methods, which are typically limited to frequencies below a few hundred megahertz by the qubit coherence times [31].

Dressed dephasing arises when frequency noise at the cavity-qubit detuning drives photon exchange between the qubit and the cavity. When the qubit is initialized in the ground state and the cavity is populated by a single photon, the dressed-dephasing induced loss rate is given by [28]

$$\kappa_{\text{dd}} = 4 \frac{g^2}{\Delta^2} S_{\delta\omega}(\Delta), \quad (1)$$

where  $g$  is the qubit-cavity coupling strength and  $S_{\delta\omega}(\Delta)$  is the frequency noise PSD evaluated at the cavity-qubit detuning frequency  $\Delta \gg g$ . Since  $\kappa_{\text{dd}}$  is directly proportional to  $S_{\delta\omega}(\Delta)$ , isolating  $\kappa_{\text{dd}}$  from the total cavity decay rate would provide a direct measure of the noise at this frequency. However,  $\kappa_{\text{dd}}$  enters the total cavity decay rate  $\kappa = \kappa_{\text{dd}} + \kappa_0$  alongside the intrinsic loss rate  $\kappa_0$ , so a standard lifetime measurement alone cannot distinguish noise-induced loss from intrinsic cavity decay. To separate the two contributions, we perform repeated mid-circuit measurements of the qubit during the cavity evolution and compare two decay curves constructed from the same data. Discarding all qubit measurement outcomes yields the unconditional photon survival probability  $P_1(t) = e^{-\kappa t}$ , which reflects the total loss rate. Post-selecting on trajectories in which every qubit measurement returns the ground state discards runs in which a cavity excitation was transferred to the qubit via a dressed-dephasing event and detected by a subsequent measurement. The remaining trajectories comprise two cases: those in which the photon survived, and those in which it was lost without detection — either through intrinsic cavity decay or through a dressed-dephasing event followed by qubit relaxation before the next measurement. The conditional photon survival probability is therefore

$$P_1^g(t) = \frac{e^{-\kappa t}}{e^{-\kappa t} + (1 - \xi)(1 - e^{-\kappa t})}, \quad (2)$$

where the detection probability  $\xi$  is the fraction of photon loss events producing a detectable qubit excitation within a single measurement interval  $T_m$ :

$$\xi = \frac{\kappa_{\text{dd}}}{\Gamma - \kappa} \cdot \frac{e^{-\kappa T_m} - e^{-\Gamma T_m}}{1 - e^{-\kappa T_m}}, \quad (3)$$

with  $\Gamma$  the qubit decay rate. In the limit  $T_m \ll 1/\Gamma$ , nearly every dressed-dephasing event is detected before the qubit relaxes ( $\xi \rightarrow \kappa_{\text{dd}}/\kappa$ ), while for  $T_m \gg 1/\Gamma$ , qubit relaxation between measurements erases the signal ( $\xi \rightarrow 0$ ). A derivation

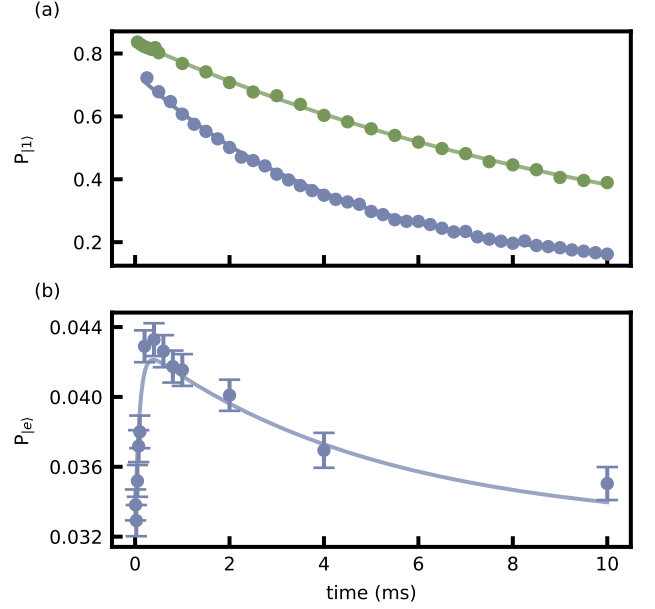


FIG. 2. Characterizing the impact of dressed dephasing on the cavity-qubit system. (a) The cavity single-photon lifetime without injected noise (green),  $T_1^c = 11.3 \text{ ms}$ , and with injected noise (blue),  $T_1^c = 4.5 \text{ ms}$ . Error bars are smaller than the markers. (b) Transmon excited-state probability as a function of time in the presence of injected noise. Dressed dephasing transfers the cavity excitation to the qubit, resulting in a temporary increase in the qubit’s excited-state population. Here, unlike the full sensing protocol (Fig. 3), the transmon population is measured only once at each wait time, without mid-circuit measurements, to directly observe the excitation transfer. The noise also induces a small steady-state increase in the transmon excited-state population. The solid line is a simulation with  $\kappa_{\text{dd}}$  as the sole free parameter, yielding  $\kappa_{\text{dd}} = (9.1 \text{ ms})^{-1}$ . All other parameters are fixed from independent measurements (Table I). Error bars represent  $\pm 1\sigma$  standard error.

of Eqs. (2)-(3) is provided in Supplemental Material V.

To realize the cavity-based sensing scheme, we integrate a transmon qubit (resonance frequency  $\omega_q/2\pi = 3.8 \text{ GHz}$ , relaxation time  $T_1^q \equiv \Gamma^{-1} = 71 \mu\text{s}$ ) with a high- $Q$  3D superconducting niobium cavity [24, 32] (resonance frequency  $\omega_c/2\pi = 4.308 \text{ GHz}$ , single-photon lifetime  $T_1^c = 11.3 \text{ ms}$ ). The transmon and cavity are dispersively coupled, with a detuning of  $\Delta = 508 \text{ MHz}$ . In addition, the transmon is dispersively coupled to a Purcell-filtered readout resonator connected to a quantum-limited amplification chain for high-fidelity single-shot readout.

To characterize the impact of dressed dephasing on the cavity, we inject controlled frequency noise into the transmon and measure the resulting change in cavity lifetime. We prepare a single photon in the cavity using a parametric sideband interaction [33, 34] (Supplemental Material IV) and drive the qubit with two noise-broadened microwave tones with amplitudes  $a_1(t)$  and  $a_2(t)$ . The beat note of the tones produces an oscillating AC Stark shift through the four-wave mixing Hamilto-

nian  $\hat{H}_{\text{noise}} \propto a_1(t)a_2^*(t)\hat{\sigma}_z$ , generating qubit frequency noise at their difference frequency (see Supplemental Material III). When this frequency matches the cavity-qubit detuning  $\Delta$ , the injected noise induces dressed dephasing and the cavity lifetime reduces from 11.3 ms to 4.5 ms (Fig. 2a).

We confirm that this increased photon loss originates from dressed dephasing by monitoring the transmon excited-state population [35] rather than the photon survival probability (Fig. 2b). The excited-state population initially rises, reflecting excitation transfer from the cavity to the qubit, and subsequently relaxes to its baseline thermal value as the added excitation dissipates. A simulation of the system dynamics with  $\kappa_{\text{dd}}$  as the sole free parameter reproduces both the lifetime reduction and the transient qubit heating (see Supplemental Material VI), indicating that dressed dephasing accounts for the observed photon loss.

Next, we benchmark the full sensing protocol using injected noise. We prepare a single cavity photon, perform repeated mid-circuit measurements of the qubit every  $4\ \mu\text{s}$  during the cavity evolution, and post-select on trajectories in which every measurement yields  $|g\rangle$  [36]. The mid-circuit measurements have no measurable effect on  $\kappa_0$  (Supplemental Material IV). Fitting both the unconditional and post-selected photon survival probabilities (Fig. 3) to Eq. (2), we extract  $\kappa_{\text{dd}} = (5.4_{-0.2}^{+0.1}\ \text{ms})^{-1}$ , consistent with the injected noise strength independently calibrated via the measured AC Stark shift (Supplemental Material III). The extracted intrinsic loss rate  $\kappa_0 = (9.7 \pm 0.4\ \text{ms})^{-1}$  indicates that the protocol correctly separates noise-induced loss from intrinsic cavity decay. The corresponding detection probability is  $\xi = 0.63$ : since the measurement interval satisfies  $T_m \ll 1/\Gamma$ , nearly ev-

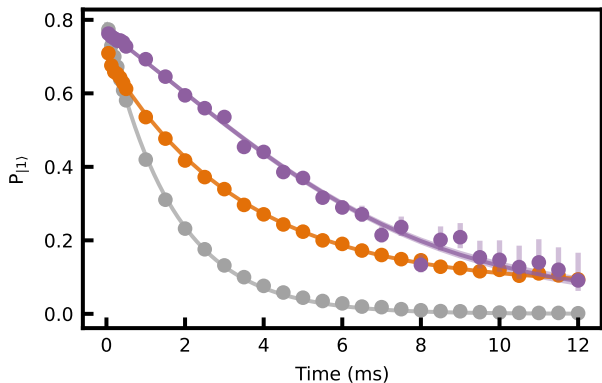


FIG. 3. Unconditional (orange)  $P_1(t)$  and post-selected (purple)  $P_1^s(t)$  single-photon survival probabilities in the presence of injected frequency noise (at a different noise amplitude than in Fig. 2). Solid lines are fits to Eq. (2) (Supplemental Material section VII) with shaded regions denoting the 68% highest density interval. Error bars are  $1\sigma$  confidence intervals. From the fit we extract  $\kappa_{\text{dd}} = (5.4_{-0.2}^{+0.1}\ \text{ms})^{-1}$ , corresponding to an induced noise PSD of  $S_{\delta\omega}(\Delta) = 293 \cdot 10^3\ \text{Hz}^2/\text{Hz}$ , and an unconditional decay rate of  $\kappa = (3.46 \pm 0.02\ \text{ms})^{-1}$ . The gray curve shows the fraction of experimental shots surviving post-selection, which decays exponentially at a rate of  $(1.7\ \text{ms})^{-1}$ , primarily due to thermal qubit excitations and false positive measurements. Each data point corresponds to 20,000 experimental repetitions.

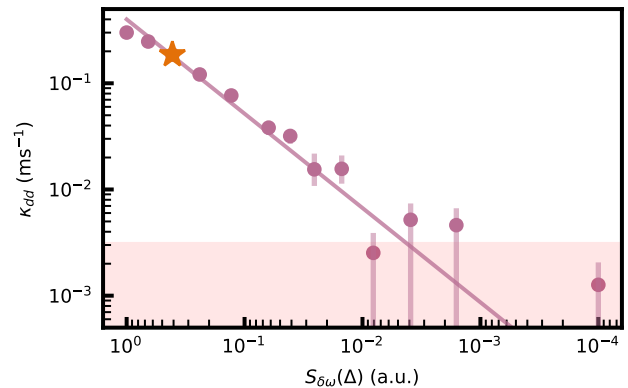


FIG. 4. Extracted dressed-dephasing rate  $\kappa_{\text{dd}}$  as a function of the injected noise PSD  $S_{\delta\omega}(\Delta)$  in arbitrary units. The fit line (pink) shows that at high noise power,  $\kappa_{\text{dd}}$  scales linearly with the noise PSD, consistent with Eq. (1). At low noise power, the extracted values plateau, and the signal is no longer resolvable. Error bars denote 68% Bayesian highest density intervals, while the shaded region (red) marks the limit of resolution. The orange star indicates the noise PSD corresponding to the data in Fig. 3. Each data point is averaged over 20,000 runs.

ery dressed-dephasing event is detected before the qubit relaxes, and  $\xi$  is limited primarily by the fraction of loss events due to dressed dephasing ( $\kappa_{\text{dd}}/\kappa$ ).

Finally, we validate the protocol by repeating it across a range of injected noise amplitudes (Fig. 4). At high noise power, the extracted  $\kappa_{\text{dd}}$  scales linearly with the noise PSD, as expected from Eq. (1). At low noise power, the extracted values plateau at a floor set by the finite statistical precision of the post-selected lifetime estimate, indicating that the noise-induced signal is no longer resolvable. Each data point is averaged over 20,000 runs; additional averaging would lower this floor accordingly. Applying the protocol without added noise, we place an upper bound of  $\kappa_{\text{dd}} < (0.29\ \text{s})^{-1}$ , corresponding to a PSD of  $S_{\delta\omega}(\Delta) < 5.4 \cdot 10^3\ \text{Hz}^2/\text{Hz}$ .

In summary, we demonstrated a cavity-based technique for sensing qubit frequency noise through photon loss induced by dressed dephasing. The key advantage of this approach is twofold: the dressed-dephasing mechanism provides direct sensitivity to noise at the cavity-qubit detuning frequency, beyond the bandwidth of conventional qubit-based spectroscopy, while the long cavity lifetime enhances the precision with which this noise can be resolved. Applying the protocol to a transmon coupled to a 3D superconducting cavity, we place an upper bound on the intrinsic dressed-dephasing rate of  $(0.29\ \text{s})^{-1}$  at 508 MHz. This frequency lies beyond the reach of existing qubit-based spectroscopy, which has probed dephasing noise up to  $\sim 300$  MHz [31].

The sensitivity of the protocol is determined by the minimum resolvable noise PSD, which scales as  $S_{\delta\omega}^{\text{min}}(\Delta) \propto \Delta^2/(g^2 T_1^c)$ . Cavity lifetimes of several seconds have been demonstrated in comparable superconducting cavities [24], which could yield up to two orders of magnitude improvement in per-shot sensitivity over the present device, potentially reaching a regime where anomalous high-frequency

noise mechanisms could be directly detected.

Additional gains can be achieved by increasing the qubit–cavity coupling strength  $g$ , provided the cavity lifetime is not compromised by the inverse Purcell effect [13], or by increasing the cavity photon number  $\bar{n}$  [30], which would require a dispersive shift large enough to resolve individual photon numbers or an alternative detection scheme for multi-photon Fock states. Integrating a flux-tunable transmon would enable the reconstruction of  $S_{\delta\omega}(\Delta)$  over a frequency range up to the GHz scale, providing a direct experimental probe of high-

frequency noise mechanisms. Such characterization could also inform background estimates for cavity-based dark matter searches [18–20], where qubit-induced dressed dephasing is a potential background that must be distinguished from candidate signals.

*Acknowledgments*— This research was sponsored by the Army Research Office and was accomplished under Grant Number W911NF-25-1-0196. S.R. is the incumbent of the Rabbi Dr Roger Herst Career Development Chair.

- 
- [1] Catelani, G., Schoelkopf, R. J., Devoret, M. H. & Glazman, L. I. Relaxation and frequency shifts induced by quasiparticles in superconducting qubits. *Phys. Rev. B* **84**, 064517 (2011).
- [2] Müller, C., Cole, J. H. & Lisenfeld, J. Towards understanding two-level-systems in amorphous solids: insights from quantum circuits. *Reports on Progress in Physics* **82**, 124501 (2019).
- [3] Yan, F. *et al.* Spectroscopy of low-frequency noise and its temperature dependence in a superconducting qubit. *Phys. Rev. B* **85**, 174521 (2012).
- [4] Bylander, J. *et al.* Noise spectroscopy through dynamical decoupling with a superconducting flux qubit. *Nat. Phys.* **7**, 565–570 (2011).
- [5] Álvarez, G. A. & Suter, D. Measuring the spectrum of colored noise by dynamical decoupling. *Phys. Rev. Lett.* **107**, 230501 (2011).
- [6] Gavrielov, N., Oviedo-Casado, S. & Retzker, A. Spectrum analysis with parametrically modulated transmon qubits. *Phys. Rev. Research* **7**, L012056 (2025).
- [7] Yan, F. *et al.* Rotating-frame relaxation as a noise spectrum analyser of a superconducting qubit undergoing driven evolution. *Nat. Commun.* **4**, 2337 (2013).
- [8] Yan, F. *et al.* Distinguishing coherent and thermal photon noise in a circuit quantum electrodynamical system. *Phys. Rev. Lett.* **120**, 260504 (2018).
- [9] Sung, Y. *et al.* Non-Gaussian noise spectroscopy with a superconducting qubit sensor. *Nat. Commun.* **10**, 3715 (2019).
- [10] Suter, D. & Álvarez, G. A. Colloquium: Protecting quantum information against environmental noise. *Rev. Mod. Phys.* **88**, 041001 (2016).
- [11] Souza, A. M., Álvarez, G. A. & Suter, D. Robust dynamical decoupling for quantum computing and quantum memory. *Phys. Rev. Lett.* **106**, 240501 (2011).
- [12] Reagor, M. *et al.* Reaching 10 ms single photon lifetimes for superconducting aluminum cavities. *Appl. Phys. Lett.* **102**, 192604 (2013).
- [13] Reagor, M. *et al.* Quantum memory with millisecond coherence in circuit qed. *Phys. Rev. B* **94**, 014506 (2016).
- [14] Krasnok, A. *et al.* Superconducting microwave cavities and qubits for quantum information systems. *Appl. Phys. Rev.* **11**, 011302 (2024).
- [15] Checchin, M., Frolov, D., Lunin, A., Grassellino, A. & Romanenko, A. Measurement of the Low-Temperature Loss Tangent of High-Resistivity Silicon Using a High-Q Superconducting Resonator. *Phys. Rev. Appl.* **18**, 034013 (2022).
- [16] Read, A. P. *et al.* Precision Measurement of the Microwave Dielectric Loss of Sapphire in the Quantum Regime with Parts-per-Billion Sensitivity. *Phys. Rev. Applied* **19**, 034064 (2023).
- [17] Alesini, D. *et al.* Galactic axions search with a superconducting resonant cavity. *Phys. Rev. D* **99**, 101101 (2019).
- [18] Braggio, C. *et al.* Quantum-Enhanced Sensing of Axion Dark Matter with a Transmon-Based Single Microwave Photon Counter. *Phys. Rev. X* **15**, 021031 (2025).
- [19] Tang, Z. *et al.* First scan search for dark photon dark matter with a tunable superconducting radio-frequency cavity. *Phys. Rev. Lett.* **133**, 021005 (2024).
- [20] Romanenko, A. *et al.* Search for Dark Photons with Superconducting Radio Frequency Cavities. *Phys. Rev. Lett.* **130**, 261801 (2023).
- [21] Agrawal, A. *et al.* Stimulated emission of signal photons from dark matter waves. *Phys. Rev. Lett.* **132**, 140801 (2024).
- [22] Berlin, A. *et al.* Searches for new particles, dark matter, and gravitational waves with srf cavities. *arXiv preprint arXiv:2203.12714* (2022).
- [23] Takenaka, T. *et al.* Three-dimensional niobium coaxial cavity with  $\sim 0.1$  second lifetime. *arXiv preprint arXiv:2510.01819* (2025).
- [24] Romanenko, A. *et al.* Three-Dimensional Superconducting Resonators at  $T < 20$  mK with Photon Lifetimes up to  $\tau = 2$  s. *Phys. Rev. Applied* **13**, 034032 (2020).
- [25] Kudra, M. *et al.* High quality three-dimensional aluminum microwave cavities. *Appl. Phys. Lett.* **117**, 070601 (2020).
- [26] Chakram, S. *et al.* Seamless High-Q Microwave Cavities for Multimode Circuit Quantum Electrodynamics. *Phys. Rev. Lett.* **127**, 107701 (2021).
- [27] Kim, T. *et al.* Ultracoherent superconducting cavity-based multiqubit platform with error-resilient control. *arXiv preprint arXiv:2506.03286* (2025).
- [28] Boissonneault, M., Gambetta, J. M. & Blais, A. Dispersive regime of circuit qed: Photon-dependent qubit dephasing and relaxation rates. *Phys. Rev. A* **79**, 013819 (2009).
- [29] Pietikäinen, I. *et al.* Strategies and Trade-Offs for Controllability and Memory Time of Ultra-High-Quality Microwave Cavities in Circuit Quantum Electrodynamics. *PRX Quantum* **5**, 040307 (2024).
- [30] Slichter, D. H. *et al.* Measurement-induced qubit state mixing in circuit QED from Up-converted dephasing noise. *Phys. Rev. Lett.* **109**, 153601 (2012).
- [31] Yoshihara, F. *et al.* Flux qubit noise spectroscopy using rabi oscillations under strong driving conditions. *Phys. Rev. B* **89**, 020503 (2014).
- [32] Milul, O. *et al.* Superconducting Cavity Qubit with Tens of Milliseconds Single-Photon Coherence Time. *PRX Quantum* **4**, 030336 (2023).
- [33] Pechal, M. *et al.* Microwave-controlled generation of shaped single photons in circuit quantum electrodynamics. *PRX* **4**, 041010 (2014).
- [34] Rosenblum, S. *et al.* A cnot gate between multiphoton qubits encoded in two cavities. *Nat. Commun.* **9**, 652 (2018).

- [35] Jin, X. Y. *et al.* Thermal and Residual Excited-State Population in a 3D Transmon Qubit. *Phys. Rev. Lett.* **114**, 240501 (2015).
- [36] Goldblatt, U. *et al.* Recovering quantum coherence of a cavity qubit coupled to a noisy ancilla through real-time feedback. *Phys. Rev. X* **14**, 041056 (2024).
- [37] Oriani, A. E. *et al.* Niobium coaxial cavities with internal quality factors exceeding  $1.4 \times 10^9$  for circuit quantum electrodynamics. *Phys. Rev. Appl.* **24**, 044080 (2025).
- [38] Heidler, P. *et al.* Non-markovian effects of two-level systems in a niobium coaxial resonator with a single-photon lifetime of 10 milliseconds. *Phys. Rev. Applied* **16**, 034024 (2021).
- [39] Johansson, J. R., Nation, P. D. & Nori, F. Qutip: An open-source python framework for the dynamics of open quantum systems. *Comput. Phys. Commun.* **183**, 1760–1772 (2012).
- [40] Abril-Pla, O. *et al.* PyMC: A modern and comprehensive probabilistic programming framework in Python. *PeerJ Comp. Sci.* **9** (2023).

## SUPPLEMENTAL MATERIAL

### I. DEVICE SPECIFICATION

The experimental device comprises three main elements: a superconducting cavity, a transmon ancilla, and a readout resonator. The cavity is fabricated from two high-purity niobium components that are electron-beam welded to eliminate seam losses and chemically etched to remove surface contamination and machining damage, enabling exceptionally long electromagnetic field lifetimes [24, 32]. A half-elliptical cavity geometry is employed to concentrate the electric field at the center of the cavity, where strong coupling to the transmon is achieved while minimizing photon loss from interactions with lossy surfaces. The aluminum transmon ancilla and readout resonator are fabricated on a sapphire chip using electron-beam evaporation. This chip is housed in a narrow coaxial waveguide and protrudes approximately 1 mm into the cavity. It is accessed via input and output couplers integrated into the waveguide. The entire device is enclosed within an aluminum shield lined with copper sheets (see Figs. 5 and 9) [37, 38].

### II. HAMILTONIAN AND PARAMETERS

We can express the free evolution of the system using the following Hamiltonian:

$$\begin{aligned} \hat{H} = & \omega_r \hat{r}^\dagger \hat{r} + \omega_q \hat{q}^\dagger \hat{q} + \omega_c \hat{c}^\dagger \hat{c} \\ & - \frac{K_r}{2} \hat{r}^\dagger \hat{r}^\dagger \hat{r} \hat{r} - \frac{K_q}{2} \hat{q}^\dagger \hat{q}^\dagger \hat{q} \hat{q} - \frac{K_c}{2} \hat{c}^\dagger \hat{c}^\dagger \hat{c} \hat{c} \\ & - \chi \hat{c}^\dagger \hat{c} \hat{q}^\dagger \hat{q} - \chi_{qr} \hat{r}^\dagger \hat{r} \hat{q}^\dagger \hat{q} - \chi_{cr} \hat{r}^\dagger \hat{r} \hat{c}^\dagger \hat{c}, \end{aligned} \quad (4)$$

where  $\hat{r}, \hat{q}, \hat{c}$  are the annihilation operators of the readout, transmon ancilla, and cavity modes, respectively. The descriptions and values of the parameters are listed in Table I.

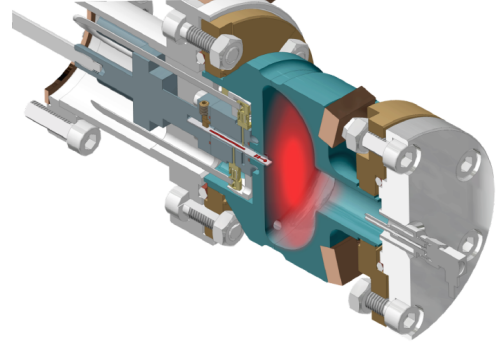


FIG. 5. Sectional view of the experimental device, showing the half-elliptical 3D niobium cavity and the transmon chip protruding into it via a coaxial waveguide.

### III. FREQUENCY NOISE INJECTION

To validate our sensing protocol, we engineer controlled frequency noise on the transmon by applying two microwave tones through its control line. The tones, with amplitudes  $\alpha_1$  and  $\alpha_2$  at frequencies  $\omega_1$  and  $\omega_2$ , produce via four-wave mixing an oscillating AC Stark shift at their difference frequency  $\Delta\omega = \omega_1 - \omega_2$ . The resulting qubit frequency fluctuation is  $\delta\omega(t) \propto a_1(t) a_2^*(t)$ , where  $a_i(t) = \alpha_i e^{i\omega_i t + i\phi_i(t)}$ . To make this shift stochastic, the phase of tone 2 is drawn uniformly at random every interval  $T = 300$  ns, while tone 1 remains coherent. Because independent phase blocks are uncorrelated, the autocorrelation of  $\delta\omega(t)$  vanishes for time separations exceeding  $T$  and decays linearly to zero within a single block. The

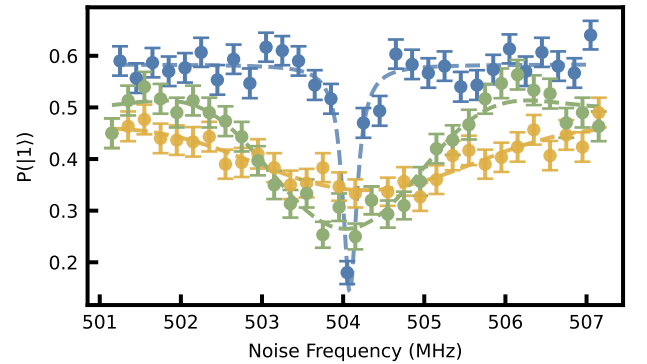


FIG. 6. Cavity photon survival probability  $P_{|1\rangle}$  as a function of the applied noise frequency, measured without phase randomization (blue) and with phase randomization every 500 ns (orange) and 200 ns (green). The main text uses a phase randomization every 300 ns. The dashed lines are fits to a Lorentzian (blue) or sinc<sup>2</sup> profiles (green, orange). Without randomization, the dip is narrow and centered at the cavity-transmon detuning  $\Delta = \omega_c - \omega_q$ , consistent with dressed dephasing. Phase randomization broadens the noise spectrum, producing a wider and shallower dip. The detuning here is  $\Delta = 504$  MHz; the main-text data were acquired at  $\Delta = 508$  MHz due to a system drift.

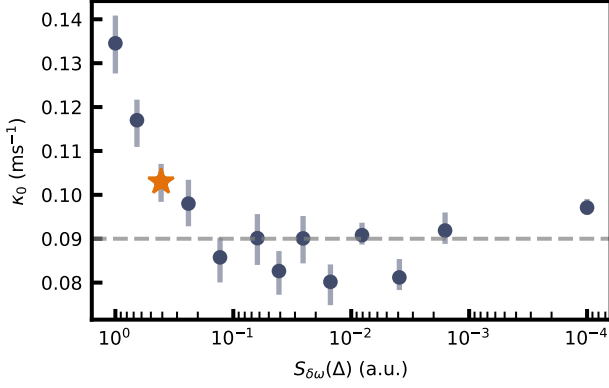


FIG. 7. Intrinsic cavity decay rate  $\kappa_0$  as a function of injected noise PSD in arbitrary units. The values for  $\kappa_0$  are extracted from the unconditional and post-selected photon survival probabilities using Bayesian inference (see Supplemental Material VII). At high noise amplitudes, we observe an increase in  $\kappa_0$  compared to the baseline value in the absence of injected noise (gray line). The noise amplitude used in Figs. 2 and 3 (orange star) was chosen to remain in the regime where  $\kappa_0$  is not significantly affected by the injected noise.

corresponding frequency-noise power spectral density is

$$S_{\delta\omega}(\omega) \propto \alpha_1^2 \alpha_2^2 T \operatorname{sinc}^2\left(\frac{(\omega - \Delta\omega)T}{2}\right), \quad (5)$$

a peak centered at  $\Delta\omega$  whose width  $2\pi/T$  is set by the phase-randomization rate and whose integrated power scales as  $\alpha_1^2 \alpha_2^2$ .

The injected noise strength can be independently calibrated from the Stark shift produced by each tone. When applied separately, each tone shifts the transmon frequency by  $\delta\omega_i \propto \alpha_i^2$ . The cross-term  $a_1 a_2^*$  that drives dressed dephasing oscillates at  $+\Delta\omega$  with amplitude  $\sqrt{\delta\omega_1 \delta\omega_2}$ , so the peak PSD is

$$S_{\delta\omega}(\Delta\omega) = \delta\omega_1 \delta\omega_2 T. \quad (6)$$

For the data in Fig. 3, the individually measured Stark shifts are  $\delta\omega_1/2\pi = 93$  kHz and  $\delta\omega_2/2\pi = 314$  kHz, yielding  $S_{\delta\omega}(\Delta) = 346 \times 10^3$  Hz<sup>2</sup>/Hz, consistent within uncertainty with the value of  $293 \times 10^3$  Hz<sup>2</sup>/Hz extracted from the sensing protocol (Fig. 3).

We calibrate  $\Delta\omega$  to match the cavity–transmon detuning by scanning  $|\omega_1 - \omega_2|$  and measuring the cavity single-photon survival probability at each value (Fig. 6); the detuning is identified as the frequency of maximum photon loss. At high noise amplitudes, we observe a reduction in the intrinsic cavity lifetime (Fig. 7), whose origin remains under investigation.

#### IV. NOISE SENSING PROTOCOL

The sensing protocol consists of three stages: initialization of a single photon in the cavity, a sequence of mid-circuit measurements during a variable wait time, and a final photon population measurement that also serves as a cavity reset.

The experiment begins with the preparation of a single-photon Fock state in the cavity. Starting from the transmon ground state  $|g\rangle$ , two consecutive  $\pi$ -pulses are applied to excite the transmon through the ladder  $|g\rangle \rightarrow |e\rangle \rightarrow |f\rangle$ . A transmon–cavity sideband drive then transfers the excitation to the cavity mode via the transition  $|f, 0\rangle \rightarrow |g, 1\rangle$  [33, 34], resonant when the sideband drive frequency satisfies  $\omega_{\text{sb}} = \omega_{ge} + \omega_{ef} - \omega_c$ , where  $\omega_{ge}$  and  $\omega_{ef}$  are the transmon transition frequencies. To verify successful excitation transfer, the transmon is measured immediately after the sideband drive. Runs in which it is not found in  $|g\rangle$  are discarded via post-selection.

Following initialization, the system idles for a variable wait time during which the transmon is measured every 4  $\mu\text{s}$ , with no effect on the intrinsic single-photon lifetime (Fig. 8). The readout discrimination threshold is set to maximize the post-selection survival fraction, with a false-positive probability of  $< 0.15\%$ , and a false-negative probability of 13%.

At the conclusion of the mid-circuit measurement sequence, the cavity population is measured and reset. A sideband drive transfers any remaining cavity excitation to the transmon, followed by sequential  $\omega_{ef}$  and  $\omega_{ge}$  pulses that return the transmon to  $|g\rangle$ . If no photon was present, the sideband drive has no effect, and the transmon ends up in  $|e\rangle$  instead. The final transmon state thus encodes the cavity population while the cavity is reset to vacuum.

#### V. DERIVATION OF THE POST-SELECTED PHOTON SURVIVAL PROBABILITY

We derive the conditional photon survival probability  $P_1^s(t)$  (Eq. (2)) and the detection probability  $\xi$  (Eq. (3)) for the mid-circuit measurement protocol.

Consider a sequence of  $N$  measurement intervals of duration  $T_m$ , with total evolution time  $t = NT_m$ . In each interval, the cavity photon decays at total rate  $\kappa = \kappa_{\text{dd}} + \kappa_0$ . If the photon is lost via dressed dephasing, the transmon is excited to  $|e\rangle$  and subsequently relaxes at rate  $\Gamma$ .

We first compute the detection probability  $\xi$ , defined as the probability that a photon lost during a single interval produces a detectable transmon excitation at the time of measurement. Given that the photon is lost during the interval, the probability density for the loss to occur at time  $\tau$  after the interval begins is  $\kappa e^{-\kappa\tau}/(1 - e^{-\kappa T_m})$ , and the loss is due to dressed dephasing with probability  $\kappa_{\text{dd}}/\kappa$ . The transmon must then remain excited for a duration  $T_m - \tau$ , which occurs with probability  $e^{-\Gamma(T_m - \tau)}$ . Integrating over all possible loss times:

$$\begin{aligned} \xi &= \int_0^{T_m} \frac{\kappa e^{-\kappa\tau}}{1 - e^{-\kappa T_m}} \cdot \frac{\kappa_{\text{dd}}}{\kappa} \cdot e^{-\Gamma(T_m - \tau)} d\tau \\ &= \frac{\kappa_{\text{dd}}}{1 - e^{-\kappa T_m}} e^{-\Gamma T_m} \int_0^{T_m} e^{(\Gamma - \kappa)\tau} d\tau \\ &= \frac{\kappa_{\text{dd}}}{\Gamma - \kappa} \cdot \frac{e^{-\kappa T_m} - e^{-\Gamma T_m}}{1 - e^{-\kappa T_m}}, \end{aligned} \quad (7)$$

yielding Eq. (3). In the limit  $T_m \ll 1/\Gamma$ , qubit relaxation is

negligible and  $\xi \rightarrow \kappa_{\text{dd}}/\kappa$ , so nearly every dressed-dephasing event is detected. In the opposite limit  $T_m \gg 1/\Gamma$ , the qubit relaxes before measurement and  $\xi \rightarrow 0$ . False negative errors are neglected in this derivation: since  $T_m \ll 1/\Gamma$ , an excitation missed by one measurement is likely to persist to the next, so the probability of eventual detection remains close to unity even for a substantial single-shot false-negative rate.

We now derive  $P_1^g(t)$ . Post-selection retains only trajectories in which every mid-circuit measurement returns  $|g\rangle$ . Within each interval, three outcomes are possible: (i) the photon survives, with probability  $e^{-\kappa T_m}$ ; (ii) the photon is lost and detected (transmon in  $|e\rangle$ ), with probability  $(1 - e^{-\kappa T_m})\xi$ , which is discarded; or (iii) the photon is lost but not detected, with probability  $(1 - e^{-\kappa T_m})(1 - \xi)$ . Once the photon is lost, no further excitations occur, and all subsequent measurements return  $|g\rangle$ . The total probability of obtaining an all- $|g\rangle$  record is therefore

$$\begin{aligned} P(\text{all } |g\rangle) &= e^{-\kappa t} + (1 - \xi) \sum_{j=1}^N e^{-\kappa(j-1)T_m} (1 - e^{-\kappa T_m}) \\ &= e^{-\kappa t} + (1 - \xi)(1 - e^{-\kappa t}), \end{aligned} \quad (8)$$

where the first term corresponds to photon survival and the sum accounts for undetected loss in each interval. The conditional photon survival probability then yields Eq. (2):

$$P_1^g(t) = \frac{e^{-\kappa t}}{e^{-\kappa t} + (1 - \xi)(1 - e^{-\kappa t})}. \quad (9)$$

## VI. SIMULATION

We simulate the joint cavity–transmon dynamics using the Lindblad master equation formalism, implemented with QuTiP [39]. The Hilbert space is truncated to at most one cavity photon and two transmon levels. The system is initialized with one cavity photon and a transmon thermal population  $n_{\text{th}}$ :

$$\rho(0) = [(1 - n_{\text{th}})|g\rangle\langle g| + n_{\text{th}}|e\rangle\langle e|] \otimes |1\rangle_c \langle 1|. \quad (10)$$

Coherent noise tones at the cavity–transmon detuning would drive a coherent excitation exchange between the two modes.

Because the phase of one tone is randomized every  $T = 300$  ns (Section III), much shorter than the system timescales, this exchange is rendered incoherent and is captured by dissipative collapse operators rather than a Hamiltonian term. The collapse operators are: cavity decay  $\sqrt{\kappa_0}c$ , transmon relaxation  $\sqrt{\Gamma}\sigma_-$ , thermal excitation  $\sqrt{\Gamma n_{\text{th}}}\sigma_+$ , pure dephasing  $\sqrt{\Gamma_\phi/2}\sigma_z$ , and dressed dephasing  $\sqrt{\kappa_{\text{dd}}}c\sigma_+$  (forward) and  $\sqrt{\kappa_{\text{dd}}}c^\dagger\sigma_-$  (reverse). The forward and reverse dressed-dephasing rates are equal by the symmetry of the injected noise spectrum; in practice the reverse process has a negligible effect since  $\kappa_{\text{dd}}/\Gamma \ll 1$ .

We compute the transmon excited-state population  $P_e(t) = \text{Tr}[|e\rangle\langle e| \rho(t)]$ , with all parameters fixed from independent measurements (Table I) except  $\kappa_{\text{dd}}$ , which is obtained by fitting the simulation to the measured  $P_e(t)$  (Fig. 2b).

## VII. BAYESIAN ESTIMATION METHODOLOGY

We extract  $\kappa_{\text{dd}}$  and  $\kappa_0$  by fitting the unconditional and post-selected decay curves simultaneously using Bayesian inference. The unconditional photon survival probability is modeled as  $P_1(t) = e^{-\kappa t}$  with  $\kappa = \kappa_{\text{dd}} + \kappa_0$ , and the post-selected probability follows Eq. (2), with  $\xi$  computed from Eq. (3). At each time point, the number of surviving photons is modeled as a binomial draw with  $n$  total trials and success probability given by the corresponding model prediction. We assign uniform priors to  $\kappa_{\text{dd}}$  and  $\kappa_0$ , and a normal prior to  $\Gamma$  centered on an independent  $T_1$  measurement with its measured uncertainty.

Posterior samples are obtained using the No-U-Turn Sampler (NUTS) with 3,000 draws and 2,000 tuning steps, implemented with PyMC [40]. All reported uncertainties are 68% highest density intervals. Posterior predictive checks confirm that the model adequately describes the data. At high injected noise amplitudes, the posterior for  $\kappa_{\text{dd}}$  is concentrated away from zero, yielding a well-resolved estimate. At low amplitudes, the posterior remains consistent with  $\kappa_{\text{dd}} = 0$ , yielding only an upper bound and defining the detection floor visible in Fig. 4.

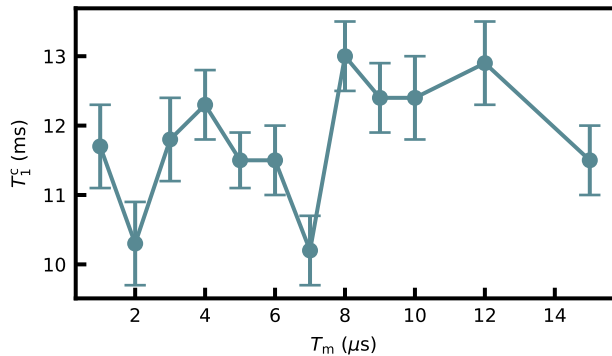


FIG. 8. Intrinsic cavity lifetime as a function of mid-circuit measurement interval duration  $T_m$ . The data confirm that the measurement protocol does not degrade the intrinsic single-photon lifetime.

Parameter	Description	Value
$\omega_c/2\pi$	Cavity resonance frequency	4.308 GHz
$T_1^c$	Cavity single-photon lifetime	$11.3 \pm 0.2$ ms
$T_2^c$	Cavity coherence time	$3.4 \pm 0.2$ ms
$\chi/2\pi$	Cavity-transmon dispersive shift	$31.7 \pm 0.3$ kHz
$g/2\pi$	Cavity-transmon coupling	6.4 MHz (*)
$\omega_q/2\pi$	Transmon resonance frequency	3.80 GHz
$K_q/2\pi$	Transmon anharmonicity	124 MHz
$T_1$	Transmon lifetime	$71.0 \pm 1.0$ $\mu$ s
$T_2$	Transmon coherence time	$35.0 \pm 2.0$ $\mu$ s
$T_{2E}$	Transmon Hahn-echo coherence time	$42.0 \pm 1.0$ $\mu$ s
$\bar{n}_{\text{th}}$	Transmon average thermal population	$2.5 \pm 0.2\%$
$\chi_{\text{qr}}/2\pi$	Transmon-readout dispersive shift	$1.05 \pm 0.01$ MHz
$\omega_r/2\pi$	Readout resonance frequency	7.82 GHz
$T_r$	Readout lifetime	$607.0 \pm 8.0$ ns

TABLE I. System parameters and their respective values. Values obtained through calculation, rather than direct measurement, are indicated with an asterisk.

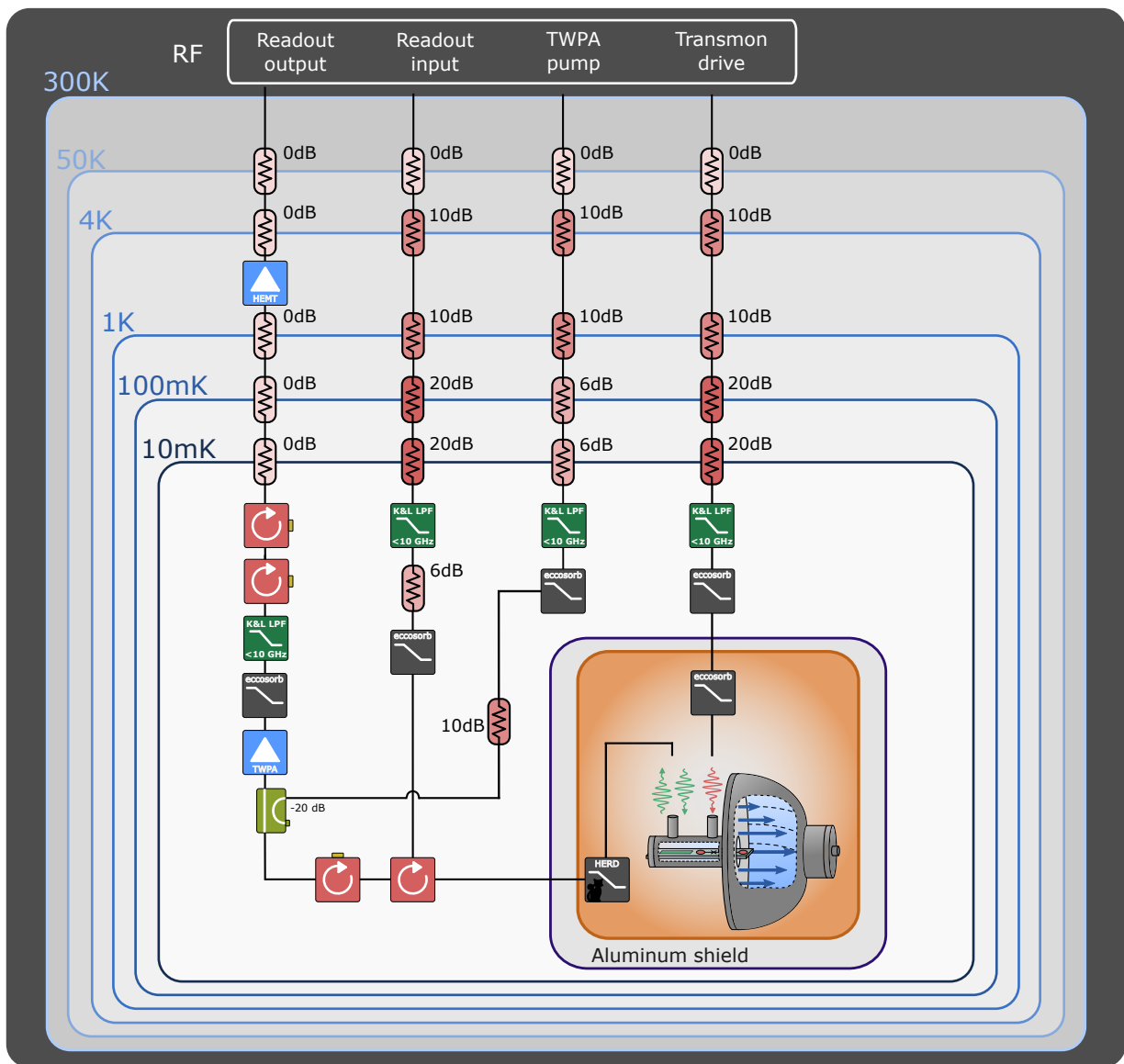


FIG. 9. Wiring diagram of the cryogenic microwave setup. The experimental device is placed inside an aluminum shield lined with copper sheets. The control signals are generated using Quantum Machines' OPX system and upconverted/downconverted using the Octave device. The signals are passed through a series of attenuators, low pass filters (LPF), and Eccosorb infrared filters. The output signal is amplified by a traveling-wave parametric amplifier (TWPA) from Silent Waves before passing through a double-junction isolator, enabling high-fidelity single-shot measurements.